Monthly Notices of the ROYAL ASTRONOMICAL SOCIETY

MNRAS **508,** 1817–1830 (2021) https://doi.org/10.1093/mnras/stab2641
Advance Access publication 2021 September 21

Galaxy and mass assembly (GAMA): The environmental impact on SFR and metallicity in galaxy groups

D. Sotillo-Ramos,[1]★ M. A. Lara-López,[2,3] A. M. Pérez-García,[4,5] R. Pérez-Martínez,[5,6] A. M. Hopkins,[7] B. W. Holwerda,[8] J. Liske,[9] A. R. López-Sánchez,[7,10,11,12] M. S. Owers[10,11] and K. A. Pimbblet[13]

[1]*Max-Planck-Institut für Astronomie, Königstuhl 17, D-69117 Heidelberg, Germany*
[2]*Armagh Observatory and Planetarium, College Hill, Armagh BT61 DG, UK*
[3]*DARK, Niels Bohr Institute, University of Copenhagen, Lyngbyvej 2, DK-2100 Copenhagen, Denmark*
[4]*Centro de Astrobiología, CAB/INTA-CSIC, ESAC Campus, Villanueva de la Cañada, E-28692 Madrid, Spain*
[5]*Asociación Astrofísica para la Promoción de la Investigación, Instrumentación y su Desarrollo, ASPID, E-38205 La Laguna, Tenerife, Spain*
[6]*ISDEFE for ESA. Camino Bajo del Castillo s/n. Urb. Villafranca del Castillo. E-28692 Villanueva de la Cañada, Spain*
[7]*Australian Astronomical Optics, Macquarie University, 105 Delhi Rd, North Ryde, NSW 2113, Australia*
[8]*Department of Physics and Astronomy, 102 National Science Building, University of Louisville, Louisville KY 40292, USA*
[9]*Hamburger Sternwärte, Universitat Hamburg, Gojenbergsweg 112, D-21029 Hamburg, Germany*
[10]*Department of Physics and Astronomy, Macquarie University, NSW 2109, Australia*
[11]*Macquarie University Research Centre for Astronomy, Astrophysics and Astrophotonics, Sydney, NSW 2109, Australia*
[12]*ARC Centre of Excellence for All Sky Astrophysics in 3 Dimensions (ASTRO-3D)*
[13]*E.A.Milne Centre for Astrophysics, University of Hull, Cottingham Road, Kingston-upon-Hull HU6 7RX, UK*

Accepted 2021 September 6. Received 2021 July 23; in original form 2021 April 28

ABSTRACT

We present a study of the relationships and environmental dependencies between stellar mass, star formation rate, and gas metallicity for more than 700 galaxies in groups up to redshift 0.35 from the Galaxy And Mass Assembly (GAMA) survey. To identify the main drivers, our sample was analysed as a function of group-centric distance, projected galaxy number density, and stellar mass. By using control samples of more than 16 000 star-forming field galaxies and volume-limited samples, we find that the highest enhancement in SFR (0.3 dex) occurs in galaxies with the lowest local density. In contrast to previous work, our data show small enhancements of ∼0.1 dex in SFR for galaxies at the highest local densities or group-centric distances. Our data indicates quenching in SFR only for massive galaxies, suggesting that stellar mass might be the main driver of quenching processes for star forming galaxies. We can discard a morphological driven quenching, since the Sérsic index distribution for group and control galaxies are similar. The gas metallicity does not vary drastically. It increases ∼0.08 dex for galaxies at the highest local densities, and decreases for galaxies at the highest group-centric distances, in agreement with previous work. Altogether, the local density, rather than group-centric distance, shows the stronger impact in enhancing both, the SFR and gas metallicity. We applied the same methodology to galaxies from the IllustrisTNG simulations, and although we were able to reproduce the general observational trends, the differences between group and control samples only partially agree with the observations.

Key words: galaxies: abundances – galaxies: fundamental parameters – galaxies: star formation.

1 INTRODUCTION

The physical processes driving the evolution of galaxies are a complex and important open question in astronomy. The role played by internal versus external processes, commonly known as nature versus nurture scenarios, has been a matter of debate for decades (e.g. Di Matteo, Springel & Hernquist 2005; Hopkins et al. 2006).

Observationally, there is evidence that between 50 and 70 per cent of the galaxy population is in groups (e.g. Eke et al. 2005). This naturally implies that processes taking place in the group environment can have a significant impact on the evolution of the galaxy population as a whole. Groups and clusters of galaxies have long been considered perfect laboratories to study the effect of feedback processes in galaxies. The effect of these processes is likely to manifest through well-known scaling relationships of galaxy properties (e.g. Tremonti et al. 2004; Lara-López et al. 2013).

With the advent of large spectroscopic surveys such as the Sloan Digital Sky survey (SDSS; Abazajian et al. 2009) and Galaxy And Mass Assembly (GAMA; Liske et al. 2015), large advancements in our understanding of the environmental processes have been made. For instance, the interplay between the stellar mass ($M_\star$) and the gas metallicity (Z) in star forming (SF) galaxies is shown to have a very strong correlation, with massive galaxies showing higher metallicities than less massive galaxies, as quantified through the M–Z relation (e.g. Lequeux et al. 1979; Tremonti et al. 2004). The M–Z relation has been extensively studied at local redshifts (e.g. Tremonti et al. 2004; Kewley & Ellison 2008), and metallicity has been shown to evolve to lower values up to redshifts of $z \approx 0.4$ (e.g. Lara-López et al. 2009a,b, 2010; Pilyugin & Thuan 2011).

★ E-mail: diego.sr.ut@gmail.com

Since metallicity is sensitive to metal losses due to stellar winds (Tremonti et al. 2004; Spitoni et al. 2010), supernovae (Brooks et al. 2007), and active galactic nuclei (AGNs) feedback (Lara-López et al. 2019), the M–Z relation provides essential insight into galaxy formation and evolution. Furthermore, the environment also plays an important role in the gas metallicity and properties of galaxies. Galaxy interactions and mergers can cause gas inflows, morphological transformations, trigger star formation, and even lead to activity in the galactic nucleus (e.g. Barton, Geller & Kenyon 2000; Lambas et al. 2003; Nikolic, Cullen & Alexander 2004; Alonso et al. 2007; Woods & Geller 2007; Ellison et al. 2008; Davies et al. 2015; Gordon et al. 2018; Ellison et al. 2019; Pan et al. 2019; Shah et al. 2020).

Studies of galaxies in pairs and clusters have revealed the environmental effects on the M–Z relation. For instance, several authors (e.g., Kewley, Geller & Barton 2006; Ellison et al. 2008; Scudder et al. 2012, 2015) find that galaxies in close pairs are more metal poor by approximately ∼0.1 dex at a given luminosity compared to galaxies with no near companion. On the other hand, Ellison et al. (2009) find that galaxies in clusters tend to have higher metallicities by up to ∼0.04 dex when compared to a control sample of the same mass, redshift, fibre covering fraction and rest-frame $g - r$ colour. This last study emphasizes that the metal enhancements are driven by local overdensities, and not just cluster membership. In terms of redshift, in the local Universe galaxies in clusters have higher metallicities on average at given stellar mass (e.g. Peng & Maiolino 2014), but at higher redshifts the influence of environment on metallicity is not clear (Kulas et al. 2013; Shimakawa et al. 2015; Valentino et al. 2015). More recently, Wu et al. (2017) examined the M–Z relation as a function of environment based on the analysis of ∼40 000 galaxies in the SDSS, and show that the metallicity has a weak dependence on the environment. Indeed, environmental processes that trigger short-lived bursts of star formation may cause a significant, but transient, change in a galaxy's metallicity before it returns to an equilibrium metallicity (Finlator & Davé 2008).

Moreover, the study of the relationship between stellar mass and star formation rate ($M_\star$–SFR) or specific star formation rate ($M_\star$–sSFR) allows us to understand the influence of environment in the evolution of galaxies and the physical processes at the origin of the quenching of star formation. It is well known that the mass and SFR follow a tight relation for star-forming galaxies – the main-sequence (MS) relation – in both the local and high-redshift Universe, with this relation shifting to higher SFR at higher z for a given mass (e.g. Karim & Schinnerer 2011; Wuyts et al. 2011). Nevertheless, few works have focused on the influence of environment on the MS, and contradictory results have been found. Some authors (York et al. 2000; Lilly et al. 2007; Wang et al. 2018) find that star formation activity in groups and clusters is, on average, reduced with respect to field galaxies, at a given stellar mass, while Peng et al. (2010) argued that these relations do not depend on environment. Recently, Calvi et al. (2018) support the conclusion of Peng et al. (2010), suggesting that morphology drives the relation between mass and SFR, more than environment.

Furthermore, the M–SFR relation has been used in the analysis of quenching processes in galaxies, where red/quiescent galaxies are characterized by denser environments (e.g. Balogh et al. 1997; Lewis et al. 2002; Baldry et al. 2006; Peng et al. 2012; McNaught-Roberts et al. 2014). The processes involved in quenching the star formation on the other hand, are still a matter of debate, and can involve a combination of ram-pressure stripping, starvation, harassment, and mergers (e.g. Gunn & Gott 1972; Moore et al. 1996; Schawinski et al. 2014; Peng, Maiolino & Cochrane 2015; Trussler et al. 2020). Alternatively, a scenario of *in situ* evolution could play a role, where passive early-type galaxies may have evolved early and rapidly within dense environments, while present-day star-forming galaxies in low-density regions have evolved more slowly, and are yet to be quenched (e.g. Wijesinghe et al. 2012).

Low mass galaxies, however, may be characterized by a delayed-then-rapid quenching scenario, initially proposed for satellite galaxies in clusters (e.g. Wetzel et al. 2013; Oman & Hudson 2016), and recently confirmed by Moutard et al. (2018) up to redshifts ∼0.6. In this scenario, the star formation is suppressed for ∼0.4 Gyr, and associated with a further morphological transformation. On the other hand, Corcho-Caballero, Ascasibar & López-Sánchez (2020) suggest an interpretation of the M–sSFR relation in terms of a single population of galaxies at different 'ageing' stages, in contrast to the bimodal picture of active and passive galaxies separated by quenching processes.

The M–Z, M–SFR, and M–sSFR relations have also been studied by means of cosmological simulations. For instance, Furlong et al. (2015) used the EAGLE (Evolution and Assembly of GaLaxies and their Environments; Schaller et al. 2015) simulation to study the M–SFR relation and the evolution of Z and SFR with time. Compared to observations, they find similar trends but a discrepancy for all ranges of mass and redshift. Davé et al. (2017), making use of the MUFASA simulation (Galaxy Formation Simulations With Meshless Hydrodynamics; Davé, Thompson & Hopkins 2016), find that galaxies with lower metallicities exhibit higher specific star formation rates, for fixed stellar mass. De Rossi et al. (2018) come to similar results with the EAGLE simulation. Bahé et al. (2017), in an analysis similar to that presented in this work, used the same simulations to compare metallicities of satellites and field galaxies, for a fixed redshift z=0.1. They find similar discrepancies with the observations and also an excess in the metallicity of satellite compared to field galaxies.

This paper introduces the relationships of mass, metallicity, SFR, and specific SFR for galaxies in groups in the GAMA survey. In Section 2 we detail the data used for this study. In Section 3.2 we introduce the M–Z relation for GAMA, and present the M–SFR and M–sSFR in Section 3.3. In Section 4 we discuss the environment influence on these relations and in Section 5 we apply a similar procedure to galaxies from a cosmological numerical simulation. Finally, in Section 6 we present a summary of our findings.

2 SAMPLE SELECTION

GAMA is a spectroscopic survey using data taken with the 3.9 m Anglo-Australian Telescope (AAT) using the 2dF fibre feed and AAOmega multi-object spectrograph (Sharp et al. 2006), the spectra were taken with 2 arcsec diameter fibres, a spectral coverage from 3700 to 8900 Å, and spectral resolution of 3.2 Å. For further details see Baldry et al. (2010), Driver et al. (2011), Hopkins et al. (2013), Liske et al. (2015).

GAMA has surveyed a total of ∼286 deg^2 split into five independent regions; three equatorial (called G09, G12, and G15), and two southern (G02, G23) fields. GAMA-I refers to a subset of data from the equatorial regions, and GAMA-II to the full five regions, see Liske et al. (2015) for further details. In this paper, we are using GAMA-II data for the three equatorial regions. For the equatorial regions G09, G12, and G15, spectra and redshifts are available for a high redshift completeness of 98.48 per cent of the galaxies within $r < 19.8$ (Liske et al. 2015).

Galaxies in groups and clusters were selected from the GAMA Galaxy Group Catalogue (G^{3}C) described in Robotham et al. (2011). The G^{3}C catalogue uses a Friends-of-Friends (FoF) algorithm, which

Table 1. For every volume-limited sample: redshift median and range, magnitude limit, number of galaxies and mass median and range (95 per cent highest density interval).

Volume	Redshift range	Redshift median	Magnitude limit (M_r)	# of galaxies	Median [log($M_\odot$)]	Mass HDI95 per cent [log($M_\odot$)]
V1	0.04–0.13	0.0854	− 19.1	352	9.71	9.07–10.57
V2	0.13–0.225	0.1836	− 20.4	299	10.06	9.59–10.76
V3	0.225–0.36	0.2925	− 21.6	105	10.64	10.17–10.11

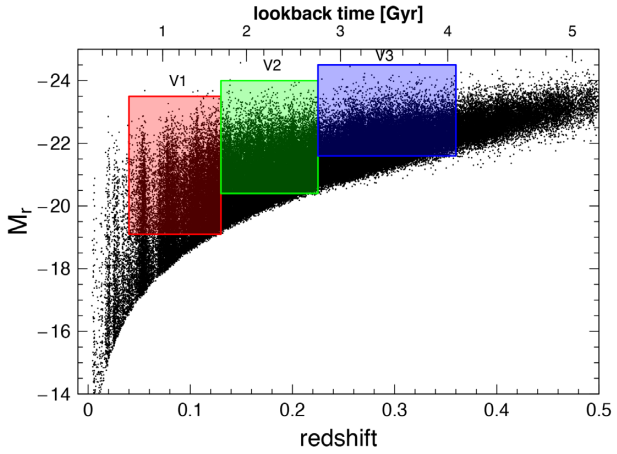

Figure 1. Selected volume-limited samples for the GAMA survey. Values for the redshift and magnitude limits are shown in Table 1.

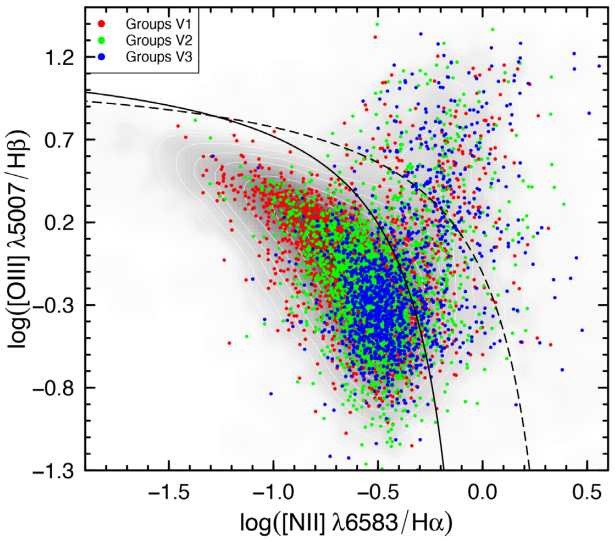

Figure 2. BPT Diagram for the GAMA spectroscopic sample. The solid line shows the Kauffmann et al. (2003) empirical division between SF and Composite galaxies, and the dashed line represents the Kewley et al. (2001) starburst limit. The red, green, and blue dots represent group galaxies in the volume-limited samples V1, V2, and V3, respectively. The grey background shows the full GAMA sample.

has been extensively tested on semi-analytic derived mock catalogues (see also Merson et al. 2013), and has been designed to be extremely robust to the effects of outliers and linking errors. In our analysis, a lower bound of groups with at least six galaxies has been set (this allows us to calculate the projected galaxy number density Σ_5 to study the local environment).

The spectroscopic data used in this paper are taken from the SpecLineSFRv05 GAMA catalogue, which includes the equivalent widths and Gaussian line flux measurements for the most prominent emission lines in GAMA-II spectra. For further details see Gordon et al. (2017). Emission line measurements are in agreement with an earlier emission line catalogue from GAMA-I Hopkins et al. (2013) using the Gas AND Absorption Line Fitting algorithm (GANDALF; Sarzi et al. 2006).

All emission line fluxes were extinction corrected using the Balmer decrement, assuming Case B recombination (Osterbrock 1989), H α/H $\beta = 2.86$, and the extinction law of Cardelli, Clayton & Mathis (1989). When H α/H $\beta < 2.86$ no correction is applied.

To avoid biases in volume and evolutionary effects due to redshift, we constructed three volume-limited samples (V1 to V3), by setting limits in M_r and redshift as indicated in Table 1 and Fig. 1. This will not alter the multiplicity (total number of galaxies per group from G^{3}C) of a given galaxy, but can imply that some of the galaxies are excluded from further statistical analysis. For reliable metallicity and SFR estimates, we selected galaxies with a signal-to-noise ratio (SNR) of 3 in H α, H β, [O III]λ5007, and [N II]λ6583. We selected star-forming galaxies using the BPT diagram (Fig. 2; Baldwin; Phillips & Terlevich 1981), and the criteria of Kauffmann et al. (2003). Galaxies classified as Composite and AGNs were selected following the criteria of Kewley et al. (2001). The total number of SF, Composite and AGN galaxies in each volume limited sample is listed in Table 2. There are a total of 756 group galaxies classified as SF in the final sample.

Table 2. Total number of star-forming, AGN, and composite galaxies.

Volume	SFG	Composite	AGN	Total
V1	2298	215	100	2613
V2	2123	298	118	2539
V3	933	222	159	1314
Total	26174	2556	1343	30073

Stellar masses were estimated by Taylor et al. (2011) (StellarMassesv19 GAMA catalogue), who estimate the stellar mass-to-light ratio (M_*/L) from optical photometry using stellar population synthesis based on the Bruzual & Charlot (2003) models. Fig. 3 shows the mass distribution for each volume sample.

Metallicities were estimated only for SF galaxies using the extinction-corrected fluxes, and the empirical calibration provided by Pettini & Pagel (2004) between the oxygen abundance and the O3N2 index:

$$\mathrm{O3N2} \equiv \log\left(\frac{[\mathrm{O\,III}]\,\lambda5007\,/\mathrm{H}\beta}{[\mathrm{N\,II}]\,\lambda6583\,/\mathrm{H}\alpha}\right). \quad (1)$$

Finally, metallicities were recalibrated to the Bayesian system of Tremonti et al. (2004) using the calibration of Lara-López et al. (2013).

Star formation rates (SFR) were estimated following Gunawardhana et al. (2011), using the equivalent width (EW) of H α to estimate

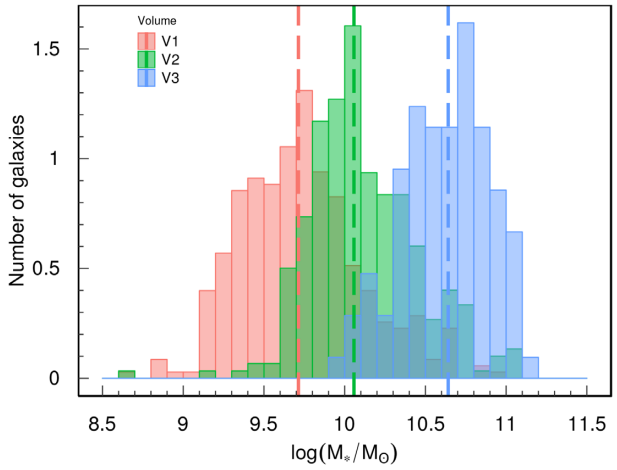

Figure 3. Mass histograms for all three volume-limited samples. Same colour coding as in Fig. 2. The dashed lines represent the median of each volume sample.

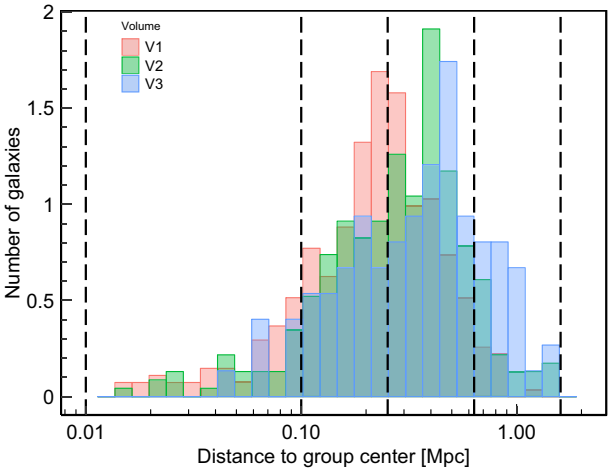

Figure 5. Distances to group centre. The dashed lines represent the limits of the four ranges used in Section 4.

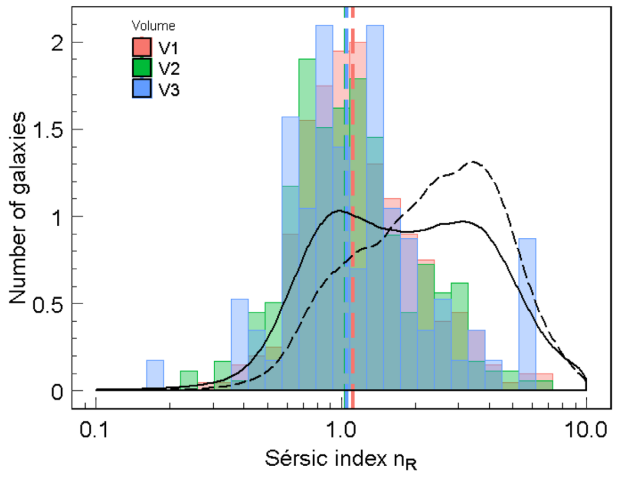

Figure 4. Sérsic index histogram for the *R*-band. The volume-limited samples V1, V2, and V3 for star-forming galaxies are shown in red, green, and blue, respectively. The solid contour shows the distribution for the whole GAMA sample, while the dashed contour for all galaxies in groups.

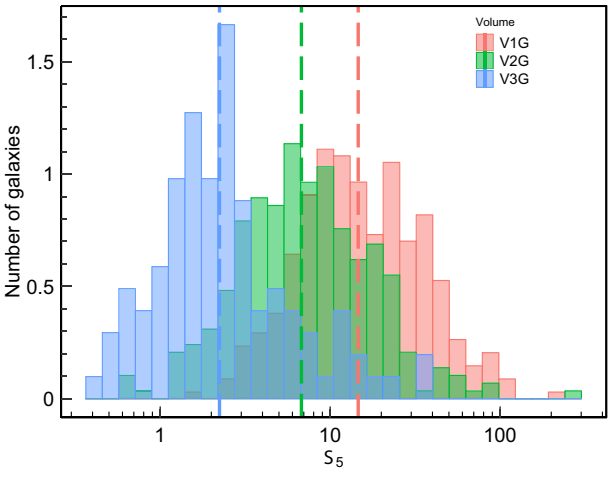

Figure 6. Distribution of Σ_5 for all three volume-limited samples. Same colour coding as in Fig. 2. The dashed lines represent the medians of each volume-limited sample.

the luminosity, correcting for aperture effects, obscuration, and stellar absorption.

To detect any possible change in the metallicity and SFR of group galaxies, a control sample of field galaxies was constructed for each volume-limited sample with the same redshift, *r*-band magnitude, and stellar mass ranges, following a similar approach to Kewley et al. (2006) and Ellison et al. (2009).

Since we aim to analyse the gas metallicity of group galaxies, our sample is composed of SF galaxies with emission lines, biasing our sample to late-type galaxies as seen in the Sérsic index distribution of Fig. 4. The same figure shows the distribution for the whole GAMA sample, and for all group galaxies. As expected, group galaxies in general show a higher proportion of early-type morphologies, consistent with Postman & Geller (1984), Dressler et al. (1997), Postman et al. (2005), Bamford, Milvang-Jensen & Aragón-Salamanca (2007), Calvi et al. (2012), among others.

Finally, to further characterize our sample, the histogram in Fig. 5 shows the distribution of galaxy distances to the group centre for our three volume-limited samples. To quantify the influence of local environment (see Section 4), we estimated the surface number density of galaxies Σ_5, as defined by Muldrew et al. (2011). The area used to calculate Σ_5 was that of the circle with radius equal to the projected distance to the fifth nearest neighbour galaxy. The final distribution of Σ_5 is shown in Fig. 6.

It is worth noting that our final sample is formed only by SF galaxies, with at least four emission lines (H α, H β, [N II]λ6583, and [O III]λ5007) to estimate gas metallicities. This biases our sample to late-type morphologies as indicated by their Sérsic index. As a consequence, passive galaxies are not included in our sample. Moreover, as seen in Fig. 5 our final sample has very few galaxies close to the group centre. This is a result of the absence of passive galaxies, given the spatial distribution expected from morphology–density relation (e.g. Dressler 1980; Goto et al. 2003).

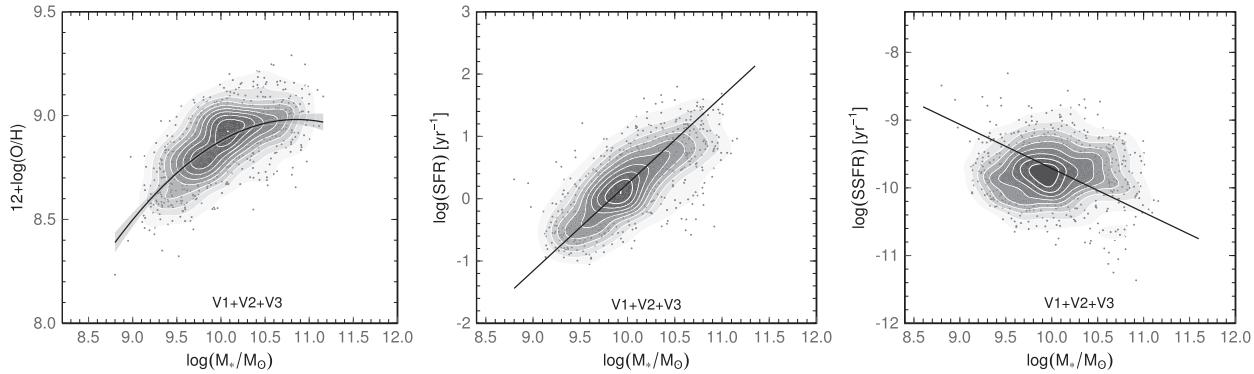

Figure 7. M–Z (left-hand panel), M–SFR (centre), and M–sSFR (right-hand panel) relations for the joint control sample. The dots represent control galaxies for the V1, V2, and V3 volumes together, and the data density is represented with the shaded areas. The solid black lines are the best-fitting relations, or the fiducial fit, also shown in grey dashed lines in Fig. 8.

3 SCALING RELATIONSHIPS FOR GALAXY GROUPS

3.1 Methodology

To detect a reliable measurement of the enhancement or suppression of SFR and metallicity in group galaxies, we follow a similar methodology to Ellison et al. (2008) and Garduño et al. (2021) and generate control samples to be taken as a reference for each subsample of galaxy groups. To obtain reliable control samples to quantify any effect due to metallicity evolution (Lara-López et al. 2009a,b; Pilyugin & Thuan 2011; Pilyugin et al. 2013) and the intrinsic shape of the each scaling relation, it is important to compare each relation of group galaxies with its respective counterpart of control galaxies in the same redshift and stellar masses ranges.

To generate control samples, first we create a field galaxy catalogue by removing galaxies in pairs and groups from our main GAMA spectroscopic catalogue. This results in a sample of ∼16 457 field galaxies. Secondly, for each galaxy in our group sample, we follow an iterative process that finds matches in redshift and stellar mass from the field galaxy sample. The iteration process finishes when the redshift and stellar mass distribution of the control sample matches the group sample (see inset histograms in Figs 8 and 10).

We create a control sample for each of the three volume-limited data sets described above (see also Fig. 1). Since every volume-limited sample spans different stellar mass ranges, in order to properly fit the shape of the scaling relationships, we created a fiducial fit to the three volume-limited samples together (V1+V2+V3).

The M–Z, M–SFR, and M–sSFR relations for the three joint control samples are shown in Fig. 7. With the above argument in mind and following a similar approach to Lara-López et al. (2013), we fit the M–Z relation of the control sample for all galaxies in all three volume-limited samples using a second-order polynomial. The fitting is done by iteratively re-weighted least-squares (IRLS).

We repeat the same procedure for the M–SFR and M–sSFR using a one-order polynomial. The coefficients of the resulting fits are given in Table 3. For the one-order polynomials, the fitting is performed with the hyper-fit routine in R (Robotham & Obreschkow 2015). Hyper-fit converts D-dimensional data with Gaussian uncertainties to a (D-1)-dimensional hyperplane with intrinsic scatter, using a maximum-likelihood approach.

The fiducial fit to the joint set of the three volume samples will function as a base fit, and will be used to measure offsets as indicated in the next section.

Table 3. From top to bottom, best-fitting coefficients for the M–Z ($12 + \log(O/H) = a + bx + cx^2$), M–SFR ($\log(\mathrm{sSFR}) = a + bx$) and M–sSFR ($\log(\mathrm{sSFR}) = a + bx$) relations. In all cases $x = \log(M_\star/\mathrm{M}_\odot)$.

Relation	a	b	c
M–Z	-7.50 ± 1.76	3.04 ± 0.35	-0.140 ± 0.018
M–SFR	-13.95 ± 0.47	1.415 ± 0.046	–
M–sSFR	-4.22 ± 0.79	-0.555 ± 0.079	–

3.2 The M–Z relation for galaxy groups

In this section we use the M–Z relation for the three joint control samples (described above) as a baseline. Next, we proceed to fix the b and c coefficients of the fiducial fit for the M–Z relation, and then fit the zero-point a separately for the group and the control galaxies for each volume-limited sample, as shown in Fig. 8. As indicated in the same figure, the coloured line corresponds to the groups, the black solid line to the control samples, and the dashed grey line is our fiducial fit.

From the fitting procedure described above, we define the difference $\Delta Z = a_{\mathrm{group}} - a_{\mathrm{control}}$, as the difference in the fitted zero points of the M–Z relation.

Confidence intervals for the differences of the zero-point coefficients are calculated using bootstrapping. We create 1020 artificial subsamples through random selection with replacement from the original samples, using the same fitting technique to estimate the coefficient a as described above, with the range of offset found taken to be the uncertainty in the measurement. The offsets in ΔZ are shown in Fig. 9 and their values together with the uncertainties are given in Table 6.

It is important to take into account that each of the samples V1 to V3 are sampling different ranges of stellar mass, since their member galaxies are selected in different magnitude limits (see Fig. 3 and Table 1). For low redshift galaxies at low stellar masses, V1, our data suggests that group galaxies show a small increment of ∼+0.04 dex in metallicity with respect to the control sample (refer to table 6 for errors). Our results for the local volume V1 are consistent with Ellison et al. (2009), who found ∼+0.05 dex higher gas metallicity for a sample of cluster galaxies in the SDSS survey.

On the other hand, for the intermediate volume V2, there is no difference in gas metallicity between control and groups. More massive galaxies in groups at higher redshifts, V3, show a very small decrement of ∼−0.024 dex in their gas metallicity with respect to the control sample. These differences are shown as purple squares

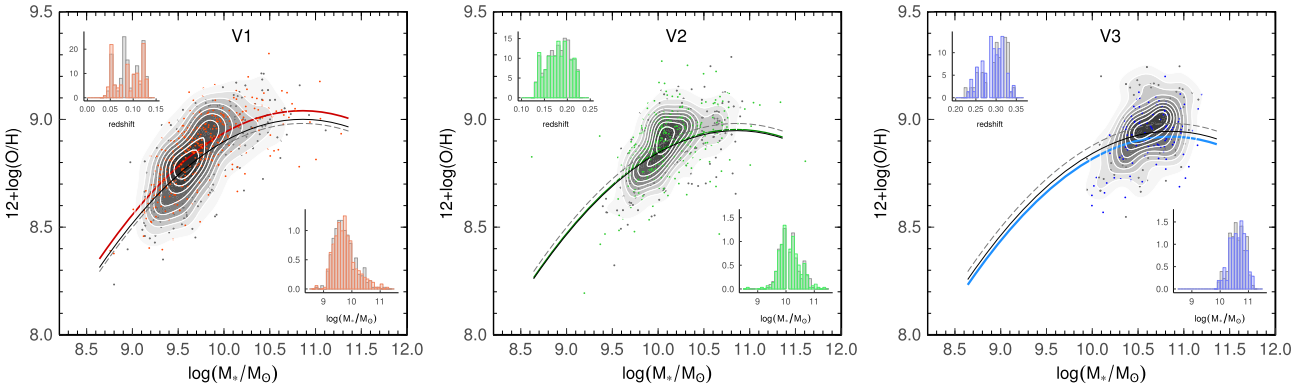

Figure 8. M–Z relations for our three volume-limited samples V1, V2, V3 (left-hand panel, centre, right-hand panel, respectively). The grey dots represent control galaxies (with the shaded areas as the data density), while coloured dots denote group galaxies. The red colours (dots, solid line fit, and histogram) correspond to galaxies in groups in the volume-limited sample V1; similarly, green for V2, and blue for V3. The black solid line represents the best fit for the control subsample, whereas the grey dashed line is the fiducial fit to all control samples. Inset histograms represent the redshift (upper) and mass (lower) distributions of the groups (coloured) and control (grey) samples.

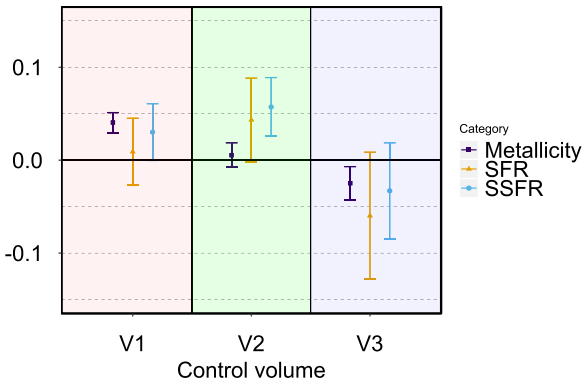

Figure 9. Differences for the zero-point coefficient between groups and control galaxy samples, in metallicity, SFR, and sSFR. Median and error bars of one standard deviation are represented.

in Fig. 9. We highlight that since the total number of galaxies in the volume V3 are ∼100, the error bars for the offsets in this volume are larger, and they must be considered with caution.

3.3 The M–SFR and M–sSFR relations for galaxy groups

We now repeat the above analysis but for the relations between the stellar mass with SFR and sSFR for our samples.

Following the same procedure described above, we fix the *b* coefficient of the M–SFR and M–sSFR relations, and fit the zero-point *a* separately for the group and the control galaxies of each volume sample (see Fig. 10). As in the M–Z diagrams, the group and control population are shown for the three volumes, together with the best fit for M–SFR and M–sSFR in each. The fiducial fit of the joint set of the control sample and the distribution of mass and redshift for the different subsamples are represented as well. While the M–sSFR relation shows a large scatter, the derived fit is the most optimal.

Significant differences in the measured zero-point coefficient can be seen for SFR and sSFR in the different subsamples (yellow triangles and blue circles, respectively, in Fig. 9). For the V1 volume there is no difference for SFR, but sSFR is marginally higher in group galaxies with respect to field galaxies. In the intermediate range of redshifts of V2, there is a clear increment in both SFR and sSFR, whereas those (more massive) galaxies in groups at higher redshifts, V3, show a slight decrement in their SFR and sSFR with respect to field galaxies.

This is consistent with a scenario where the environmental mechanisms enhancing the star formation, mainly galaxy–galaxy interactions, are noticeable at the redshift range of V2. The processes quenching star formation (starvation, harassment), need longer times to produce observable effects and become dominant at the redshift of V1.

Despite the larger uncertainties, the lower SFR and sSFR obtained for galaxies in the V3 volume (that are in general more massive as showed in Fig. 3) agrees with previous work (von der Linden et al. 2010; Vulcani et al. 2010; Allen et al. 2016).

A decrease in SFR and sSFR in galaxy groups could be originated as a result of a morphology-driven quenching process, as suggested by Calvi et al. (2018). To test this hypothesis, in Fig. 4 we show a comparison of the Sérsic index for group and control galaxies for every one of our three volume-limited samples. For the same samples, Table 4 indicates the percentage of galaxies with Sérsic index lower and higher than 2, which is our threshold to divide late from early-type morphologies. From Table 4 it is evident that group and control galaxies have very similar percentages. The V3 sample shows the highest percentage of early-type galaxies, however, the percentage of both, group and control in V3 are consistent within 1 per cent. Histograms for the Sérsic index distributions are shown in Fig. 11 for control and group galaxies for each volume, in each case following similar distributions. We quantify also the possible differences on the means of the distributions by running a *t*-test for each volume. For a 95 per cent confidence level, we cannot reject the null hypothesis of both samples (group and control) having the same distribution. Hence, we discard a morphological driven quenching, since both, control and group galaxies show similar morphologies at given volume. Again, we highlight that this study is focused on Star Forming galaxies with at least four emission lines, and a morphology driven quenching process can still be happening in galaxies that were cut-off form our sample.

4 HOW MUCH DOES ENVIRONMENT AFFECT THE PROPERTIES OF GALAXIES?

In this section, we analyse variations in metallicity and star formation rate in new subsamples created taking into account the distribution

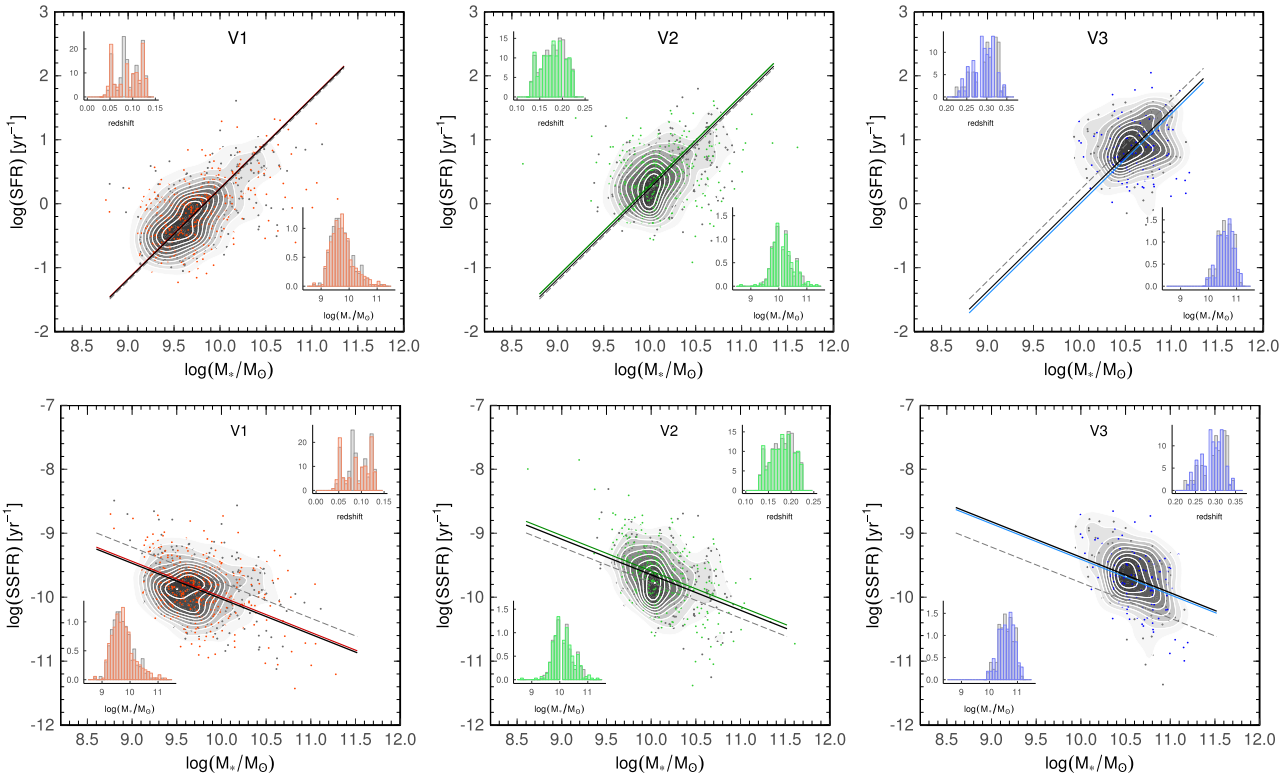

Figure 10. M–SFR and M–sSFR relations for our three volume-limited samples V1, V2, V3 (left-hand panel, centre, right-hand panel, respectively). The grey dots represent control group galaxies, coloured dots (red, green, blue for V1, V2, V3, respectively), group galaxies. The black line represents the best fit for the control subsample whereas the coloured line is the fit for the group galaxies subsample. The grey dashed line is the fiducial fit to the joint set of the control sample. Inset histograms represent the redshift (upper) and mass (lower) distributions of the groups (coloured) and control (grey) samples.

Table 4. Comparison of Sérsic index for groups and control galaxies. From left to right, volume sample, total number of galaxies in each volume, percentage of galaxies with Sérsic index lower than 2 (late-type morphology) and higher than 2 (early-type morphology).

Volume	# of Galaxies	$n_R < 2$ (per cent)	$n_R > 2$ (per cent)
V1 Groups/Control	352/358	68.5/68.7	14.5/10.9
V2 Groups/Control	299/322	72.0/70.5	15.7/12.4
V3 Groups/Control	105/128	65.7/72.6	16.2/17.2

of group members, distance to the group centre, Σ_5, and stellar mass, as explained below.

First, to understand the general scope of the data, we combine the three volumes described above into one single sample. We divide the combined sample into four bins of distance to the centre of the group (R1 to R4, see Fig. 5), where R1 ranges from 0.01 to 0.1 Mpc, and R2 to R4 are equally spaced logarithmically, from 0.1 to 1.6 Mpc, as shown in Fig. 12. Our results indicate small variations in gas metallicity for group galaxies with respect to the field, with a maximum difference of ~ -0.05 dex ($\sim 2\sigma$) for galaxies in the most distant bin. In contrast, we always find increments in SFR (and sSFR) with respect to the control sample of field galaxies at all distances, where the smallest increment corresponds to the closest distance bin, and the largest the two intermediate bins. The low metallicity and high SFR in the more distant bin is likely to be related to the presence (or accretion) of H I rich galaxies residing preferentially in the outskirts of groups (e.g. Hess & Wilcots 2013).

Other authors find that the SFR is suppressed near the centre of groups and clusters (e.g. Poggianti et al. 1999; Couch et al. 2001; Barsanti et al. 2018). Our results indicate however, a small increment of 0.1 dex for the most central group galaxies in our sample. To understand the origin of this discrepancy, it is important to bear in mind that our sample is composed only of SF galaxies, and selected to have at least four emission lines to be able to estimate SFRs and gas metallicities. As already noted, these requirements bias our sample to late-type galaxies (see Fig. 4), decrease the number of galaxies sampled near group centres, and prevent the inclusion of low-SFR, mostly quenched, and passive galaxies that might otherwise decrease the average SFR of our samples near the group centre. Additionally, some effect may be contributed by the different way of selecting control samples. For instance, some authors compare group with field galaxies without further matching for stellar mass or redshift (e.g. Vulcani et al. 2010). Nevertheless, proper control samples are necessary to establish robust differences (e.g. Ellison et al. 2009).

To better quantify the influence of local environment, we use the surface number density (Σ_5) (Muldrew et al. 2011). From the combined sample, we created four bins (D1 to D4) of 0.5 dex covering the total range of values from 0.1 to 100, and estimated the differences in Z, SFR, and sSFR, as shown in Fig. 13. Our data shows enhanced SFRs in group galaxies for all the Σ_5 bins. The differences in SFR and sSFR decrease when increasing the surface density, reaching values slightly higher (but still below 0.1 dex) in the bin with the highest Σ_5.

This supports the accelerated evolution scenario ('*in situ* evolution') in groups. The differences in SFR and sSFR in the group

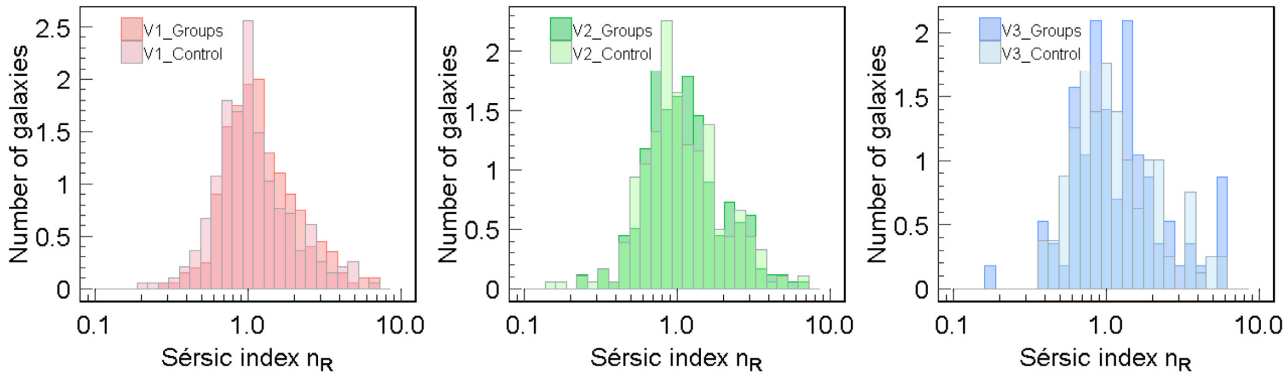

Figure 11. From left to right, Sérsic index histograms for samples V1, V2, and V3. The light and darker colours in each panel correspond to Control and Group samples, respectively.

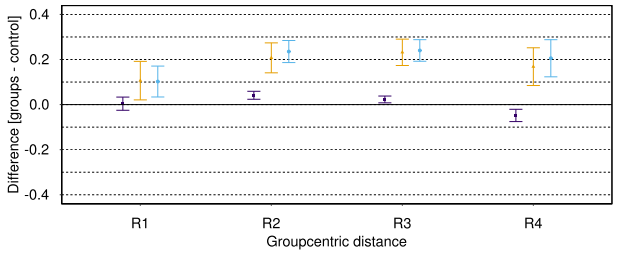

Figure 12. Differences for the zero-point coefficients in metallicity, SFR and SSFR (colour code as in Fig. 9) between groups and control galaxy samples for all three volumes grouped. The median and error bars of one standard deviation are represented for four ranges of group-centric distance from low to high.

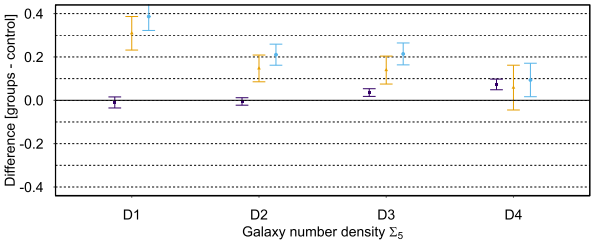

Figure 13. Differences for the zero-point coefficients in metallicity, SFR, and SSFR (colour code as in Fig. 9) between groups and control galaxy samples for all three volumes grouped. The median and error bars of one standard deviation are represented for four ranges of Σ_5 density from low to high.

versus field sample in the highest density and the closest distance bins, respectively, indicate that the effect of the environment has mainly occurred as part of the infalling process.

Similarly, the metallicity found in our group sample is higher by ∼0.08 dex in the highest surface density bin, in agreement with Ellison et al. (2009), while in the rest of the bins the values are comparable with those in the field. Stripping of low-metallicity gas from the galaxy outskirts, as well as suppression of metal-poor inflows towards the galaxy centre, are key drivers of the enhancement of gas metallicity (e.g. Bahé et al. 2017).

Next, we aim to explore the effect of the stellar mass in the joint sample. Moutard et al. (2018) propose two different types of quenching of the star formation activity. A fast environmental quenching channel followed by young low-mass galaxies, $\log(M_\star/M_\odot)$ <9.7,

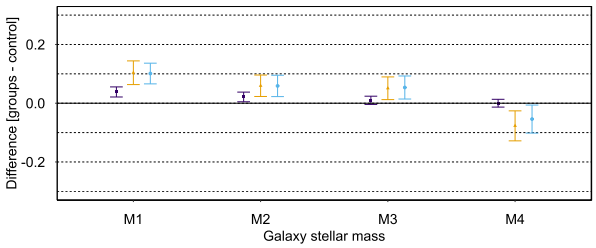

Figure 14. Differences for the zero-point coefficients in metallicity, SFR, and SSFR (colour code as in Fig. 9) between groups and control galaxy samples for all three volumes grouped. The median and error bars of one standard deviation are represented for four ranges of stellar mass from low to high.

Table 5. Interval ranges of group-centric distance, Σ_5, and stellar mass for the combination of the three volume-limited samples used if Figs 12 to 14.

	B1		B2		B3		B4		
Distance	0.01	–	0.10	–	0.25	–	0.63	–	1.60
Σ_5	0.41	–	2.07	–	10.48	–	53.12	–	269.19
Mass	8.62	–	9.70	–	9.99	–	10.35	–	11.60

and a slow quenching channel followed by more evolved higher mass galaxies. In Fig. 14 we show the differences in our combined sample divided into four mass bins as indicated in Table 5. To accurately test signs of fast quenching, our first mass bin M1 is formed by galaxies with $\log(M_\star/M_\odot) < 9.7$, as discussed in Moutard et al. (2018). Our results show a small enhancement of ∼0.1 dex for SFR and sSFR (see Fig. 14) for the lowest mass bin M1. If environmental mechanisms are the dominant channel to suppress the star formation in galaxies on a short time-scale (Moutard et al. 2018), then we should not expect any significant changes in the star formation compared to the control sample for low mass galaxies. In addition, since such galaxies would quickly be quenched and classified as passive, they would be cut out of our sample. Therefore, we do not observe signs of fast quenching in this mass range for our sample of galaxies.

For the same low mass bin in Fig. 14, we observe an increment in the gas metallicity by ∼0.05 dex, while it remains unchanged for the rest of the mas bins. This increment in metallicity has been previously observed in simulations as a signature of 'chemical pre-processing' of infalling cluster galaxies (e.g. Gupta et al. 2018). Under this paradigm, at $z < 1.0$, cluster galaxies (both already accreted and infalling) accrete gas that is 2–3 times more metal rich compared to

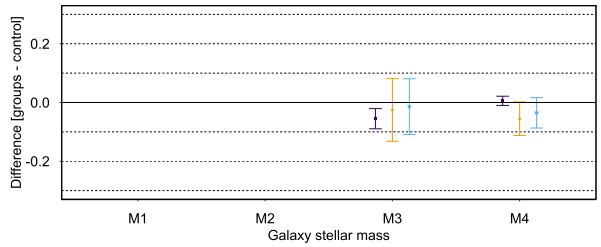

Figure 15. Similar to Fig. 14, but using a volume-limited sample with the magnitude limits of V3, see the text.

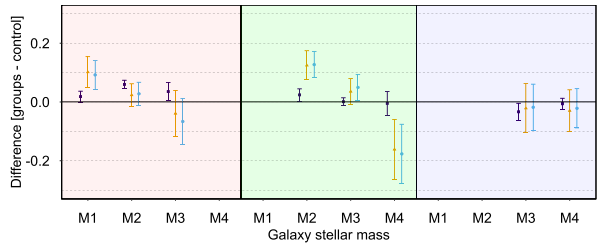

Figure 16. Differences for the zero-point coefficients between groups and control galaxy samples, in metallicity, SFR, and SSFR (colour code as in Fig. 9). The median and error bars of one standard deviation are represented. Base volumes and additional subsamples consisting of the same four bins in mass as in Fig. 14 (see Table 5).

field galaxies. Furthermore, since environmental processes are most effective for galaxies with $\log(M_\star/M_\odot) < 10$ (Peng et al. 2010), it is likely that inflow of pre-enriched gas drives the observed metallicity enhancement.

The SFR and sSFR show only small increments of ∼0.05 dex for the next mass bins M2 and M3 (see Fig. 14), while for the massive bin M4 there is a clear suppression of SFR and sSFR by ∼−0.06 dex. Even though the control samples should ameliorate any selection effect, the combination of all three volume-limited samples together could introduce a bias, since each one of them has a different luminosity and hence stellar mass limit. To control for this effect, we created a new volume-limited sample by imposing the magnitude limits of V3 on all three volume-limited samples. In this way, any luminosity or mass effects should be controlled. Naturally, this new volume-limited sample limits our data to the most massive galaxies, and hence we are only able to analyse samples M3 and M4, the result is shown in Fig. 15. We are able to recover signs of quenching for the most massive galaxies in M4, and hence corroborate the observed sign of quenching for massive galaxies.

As already mentioned, since our sample of galaxies is restricted to galaxies with at least four emission lines, we are likely missing quenching signatures from more massive and passive galaxies. Therefore, we are unable to address the transition from SF to passive galaxies and hence cannot compare our results directly with previous work in that area (e.g. Wijesinghe et al. 2012).

To observe more detailed signatures of the chemical pre-processing of infalling galaxies or other evolution, we focus now on our individual volume-limited samples. Each volume is considered individually, and divided into four equal mass bins. A summary of the mass ranges for each subsample is given in Table 6, and the differences found in Fig. 16. We find consistent enhancements in gas metallicity for the volume V1. This result is in agreement with the 'chemical pre-processing' scenario described above, where the effect of environment is stronger in low mass galaxies.

On the other hand, at all volumes, the SFR shows signs of quenching for the most massive galaxies in the bin M4 of V3. The mass range M3 do not show any clear pattern, showing a quenched SFR for volumes V1 and V3, and an enhanced SFR for V2. We do not discard however, an evolutionary effect between volumes V1 and V2, as suggested by the common mass ranges M2 and M3. These mass ranges show higher metallicities, and lower SFRs in V1, in contrast with negligibly changes in metallicity, and higher SFRs for the same mass ranges in V2

It is likely that the chemical enrichment of the intracluster medium (ICM) plays a major role in enhancing the gas metallicities of infalling galaxies, as observed in simulations (e.g. Gupta et al. 2018). On the other hand, there is evidence that the metallicity of the ICM does not evolve up to redshift $z \sim 1.0$ (McDonald et al. 2016; Biffi et al. 2017).

For a summary of the differences found in the various subsamples see Table 7.

5 SIMULATIONS

We perform a similar study using the IllustrisTNG cosmological magnetohydrodynamical simulation of galaxy formation (Marinacci et al. 2018; Naiman et al. 2018; Nelson et al. 2018; Pillepich et al. 2018; Springel et al. 2018). Following our observational analysis, we constructed similar samples in redshift and absolute magnitude to analyse variations in metallicity and SFR against stellar mass. For simulated cubic volumes of roughly 300 comoving Mpc side length, and starting with a redshift value of 127, a total of 100 snapshots (including all the information for all particles in the whole volume) of the complete temporal evolution are stored. They are separated by time-steps ranging from 50 to ≈100 Ma. The identification of haloes and subhaloes in groups is performed with a friends-of-friends algorithm. This is performed only on the dark matter (DM) particles. The other types of particles present in the simulation, which include gas, stars, or black holes, join the same group of their nearest DM particle.

We take the following approach to select the samples from the simulation. We choose the snapshot whose redshift value is closest to the median value of each of the three volume-limited samples from GAMA (Table 8). Since in GAMA we have an observational limit imposed by the instrumentation ($r < 19.8$), we have to select, for each snapshot, only the galaxies that could have been observed at their respective redshift value. Limits of absolute magnitude for the r-band are shown also in Table 8.

The resolution of the simulation will impose one limit on the galaxies that can be selected for our sample. Studies where morphological characteristics are important define a lower bound of ≈1000 (Yun et al. 2019) or 10 000 (Semczuk et al. 2020) star particles. Since we are exploring integrated properties we can set a lower limit of 10 particles, which allows us to reach a stellar mass limit in the selected galaxies as low as 10^9 $M_\odot$. This is important to enable us to analyse the less massive galaxies present in V1. Patton et al. (2020) define a lower bound of 90 star particles per galaxy in their recent studies with the IllustrisTNG300 simulation, a similar order of magnitude to ours.

Similar to the GAMA samples, we want to identify groups with at least six members. The galaxy counting for each snapshot is performed before applying the same magnitude limits of the GAMA volumes (Table 1). Additionally, we remove passive galaxies using the limit provided by Hsieh et al. (2017) in the M–SFR relation. We can apply two cuts with constant sSFR (depicted as black dashed lines in the M–SFR relation in Fig. 17). Next

Table 6. Summary of the differences found for the different subsamples. From left to right, the columns indicate the subsample, number of galaxies, median Sérsic index $\tilde{n}_r$, surface number density, median stellar mass, 95 per cent highest density interval (HDI), and difference in gas metallicity (Z), SFR, and sSFR, respectively. The first, second, and third block correspond to the V1, V2, and V3 volumes, respectively.

Subsample	No. of galaxies	Sérsic $\tilde{n}_r$	Σ_5	$\tilde{M}_\odot$	95 per cent HDI ($M_\odot$)	ΔZ	ΔSFR	ΔsSFR
V1	352	1.12	14.63	9.71	9.07–10.57	0.040 ± 0.011	0.009 ± 0.036	0.030 ± 0.031
M1	94	1.09	15.15	9.34	9.13–9.46	0.018 ± 0.019	0.102 ± 0.052	0.092 ± 0.049
M2	180	1.10	14.08	9.73	9.48–9.71	0.060 ± 0.014	0.024 ± 0.038	0.028 ± 0.039
M3	55	1.25	13.87	10.19	9.72–9.94	0.035 ± 0.031	−0.039 ± 0.079	−0.066 ± 0.078
M4	17	1.60	18.62	–	–	–	–	–
V2	299	1.05	6.81	10.06	9.59–10.76	0.005 ± 0.013	0.043 ± 0.045	0.057 ± 0.032
M1	4	3.18	5.66	–	–	–	–	–
M2	107	0.93	7.04	9.84	9.48–9.71	0.024 ± 0.021	0.125 ± 0.050	0.127 ± 0.045
M3	144	1.12	6.60	10.18	9.72–9.94	0.001 ± 0.013	0.036 ± 0.044	0.050 ± 0.043
M4	37	1.39	8.91	10.66	9.95–10.82	−0.004 ± 0.040	−0.161 ± 0.102	−0.177 ± 0.101
V3	105	1.06	2.32	10.64	10.17–11.11	−0.024 ± 0.017	−0.060 ± 0.068	0.032 ± 0.051
M1	0	–	–	–	–	–	–	–
M2	2	0.55	2.33	–	–	–	–	–
M3	33	0.85	1.82	10.37	9.72–9.94	−0.034 ± 0.030	−0.021 ± 0.084	−0.018 ± 0.079
M4	63	1.29	2.23	10.75	9.95–10.82	−0.006 ± 0.019	−0.029 ± 0.071	−0.022 ± 0.067

Table 7. Summary of the differences found for the different subsamples. Subsamples correspond to the total sample of group galaxies (V1+V2+V3). In each of the four blocks, subsamples are selected as follows: group-centric distance, surface number density, galaxy stellar mass, and galaxy stellar mass with a magnitude-cut corresponding to V3. From left to right, the columns indicate the subsample, number of galaxies, median Sérsic index $\tilde{n}_r$, median and 95 per cent highest density interval (HDI) of the parameter in consideration, and differences in gas metallicity (Z), SFR, and sSFR, respectively.

Subsample	No. of galaxies	Sérsic $\tilde{n}_r$	$\tilde{\text{Dist}}$	95 per cent HDI (Dist)	ΔZ	ΔSFR	ΔsSFR
R1	84	1.16	0.062	0.019–0.099	0.004 ± 0.029	0.106 ± 0.085	0.102 ± 0.069
R2	259	1.01	0.176	0.104–0.248	0.041 ± 0.018	0.207 ± 0.066	0.235 ± 0.049
R3	321	1.14	0.381	0.252–0.586	0.023 ± 0.015	0.2329 ± 0.058	0.240 ± 0.048
R4	63	0.94	0.820	0.638–1.438	−0.048 ± 0.027	0.168 ± 0.084	0.206 ± 0.082
Subsample	No. of galaxies	Sérsic $\tilde{n}_r$	Σ_5	95 per cent HDI (Σ_5)	ΔZ	ΔSFR	ΔsSFR
D1	112	0.96	2.176	1.094–3.008	−0.010 ± 0.025	0.309 ± 0.077	0.386 ± 0.064
D2	276	1.20	6.135	3.172–9.529	−0.005 ± 0.017	0.147 ± 0.061	0.210 ± 0.049
D3	261	1.02	16.129	10.047–27.822	0.036 ± 0.018	0.139 ± 0.064	0.214 ± 0.051
D4	82	1.13	43.214	32.043–88.228	0.073 ± 0.025	0.059 ± 0.103	0.094 ± 0.077
Subsample	No. of galaxies	Sérsic $\tilde{n}_r$	$\tilde{M}_\odot$	95 per cent HDI ($M_\odot$)	ΔZ	ΔSFR	ΔsSFR
M1	189	1.06	9.473	9.136–9.690	0.038 ± 0.017	0.104 ± 0.040	0.101 ± 0.035
M2	189	0.99	9.834	9.702–9.972	0.021 ± 0.016	0.059 ± 0.037	0.059 ± 0.036
M3	189	1.36	10.130	9.995–10.337	0.010 ± 0.014	0.051 ± 0.039	0.054 ± 0.039
M4	189	1.46	10.633	10.353–11.053	0.000 ± 0.013	−0.077 ± 0.051	−0.054 ± 0.048
Subsample	No. of galaxies	Sérsic $\tilde{n}_r$	$\tilde{M}_\odot$	95 per cent HDI ($M_\odot$)	ΔZ	ΔSFR	ΔsSFR
M1	–	–	–	–	–	–	–
M2	–	–	–	–	–	–	–
M3	21	0.80	10.24	9.999–10.333	−0.055 ± 0.034	−0.025 ± 0.106	−0.014 ± 0.095
M4	111	1.24	10.685	10.360–11.055	0.006 ± 0.016	−0.055 ± 0.057	−0.035 ± 0.052

Table 8. Redshift, luminosity distance, and absolute magnitude limits (*r*-band, according to the GAMA apparent limiting magnitude $m_r = 19.8$) for the different simulation snapshots.

Vol_G	z_G median	z_{TNG}	Snapshot	d_{lum} (Mpc)	M_r
V1	0.0854	0.08	92	358.1	−17.97
V2	0.1836	0.18	85	859.4	−19.87
V3	0.2925	0.30	78	1530.8	−21.12

we perform two different selections. For the V1 and V2 samples, galaxies with log(sSFR)>−10.6 are selected, while galaxies with log(sSFR)<−11.4 are considered passive galaxies. For the V3 volume, all galaxies with log(sSFR)<−10.6 are considered passive. This first selection provides a more complete but also more contaminated sample for V1 and V2. For the V3 volume, we get a complete and low contamination sample. Since the simulation does not allow for selecting star-forming galaxies using the BPT diagram, we have additionally matched, for each galaxy in the GAMA group samples, the closest galaxy in mass for the corresponding group samples in the simulation.

The creation of control samples requires the identification of field galaxies. Since the identification of groups in IllustrisTNG is performed with an FoF algorithm (as is also the case for the GAMA Groups Catalogue, see Section 2), all galaxies in unitary groups are included in the field catalogue. Moreover, all satellite galaxies in haloes at distances from the host galaxy larger than $4.5 \times R_{200c}$ (where R_{200c} is the radius of the sphere with a density of 200 times the critical density of the Universe), are also considered to be field

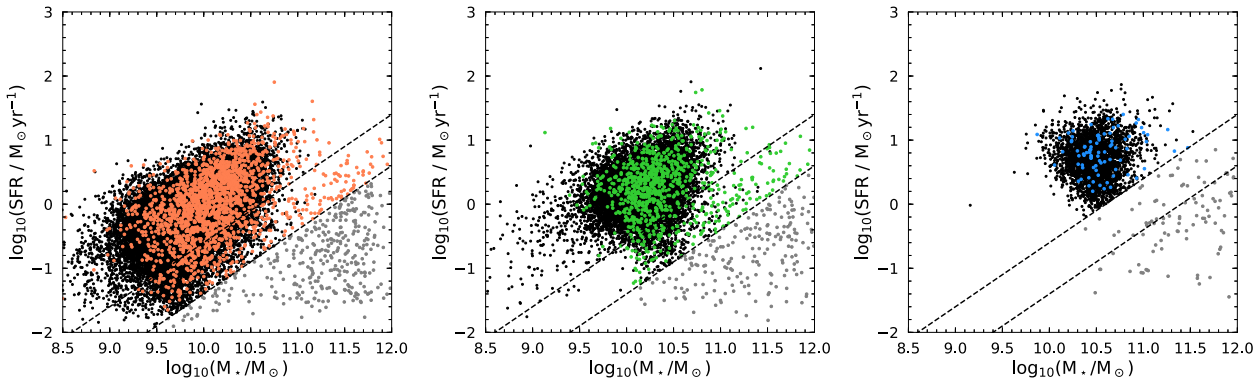

Figure 17. M–SFR relationship for our three volume samples V1, V2, V3 (left-hand panel, centre, right-hand panel, respectively) from IllustrisTNG300-2. For the star-forming sample (coloured for groups, black for field), we perform two different selections to reject passive galaxies: (*i*) all galaxies with log(sSFR) higher than −10.6 for V1 and V2, and (*ii*) all galaxies with log(sSFR) higher than −11.4 for V3. Galaxies considered passive are coloured as grey dots.

Table 9. Stellar mass statistic for the volume-limited samples.

Vol	Mass [log $M_\odot$]				
	Min	Quartile 1	Median	Quartile 3	Max
V1	8.495	9.853	10.088	10.342	12.035
V2	9.157	10.126	10.286	10.519	12.035
V3	9.870	10.420	10.521	10.683	11.470

galaxies, as suggested by Busha et al. (2005), Haines et al. (2015) and Barsanti et al. (2018).

This last step completely defines the group and field catalogues from the simulations. To define the control samples we follow the same procedure as for the observational data from GAMA. We find three matches in mass (redshift will be exactly the same for each snapshot) from the field catalogue until the mass distribution is the same for groups and field galaxies. We show stellar mass statistics for each volume in Table 9.

To calculate the M–Z and M–SFR relations we proceed as described in sections 3.2 and 3.3. The resulting M–SFR relationships for the different volumes are shown in Fig. 18, and in Fig. 19 for the M–Z relation. For the fit of the M–Z relation, the polynomial corresponding to the GAMA control sample has been taken, leaving free the constant term to match the simulation sample. The GAMA fit was used since the fit to the IllustrisTNG control galaxies is strongly affected by high mass and low metallicity galaxies (red fit in Fig. 20), that are not present in the GAMA samples. The differences in Z and SFR are summarized in the Fig. 21, represented on the same scale as Fig. 9. We only find similar trends as with the GAMA data for the volume V2. The strongest discrepancy is observed for the volume V3, which shows an enhancement in SFR, and higher gas metallicity with respect to the control sample. It is worth noting however, that V3 is also the volume with the smallest number of galaxies in both GAMA and IllustrisTNG. Furthermore, the sample of massive and low metallicity galaxies in the control sample of V3 strongly biases the fit to the zero-point, and hence the metallicity difference we measure here is not reliable.

Illustris and IllustrisTNG have successfully reproduced the observational trends for individual or small samples of groups and clusters (Genel 2016; Vogelsberger et al. 2018, respectively), and some authors have found evolutionary effects, for different redshifts, on the M–Z (Torrey et al. 2019) and M–SFR (Torrey et al. 2018; Hwang, Shin & Song 2019) relations. However, these studies explore overall values, and not differences, as we do, over a wider range of redshift, and hence a comparison with our results is not directly applicable.

To explain the discrepancies between IllustrisTNG and GAMA, we list the differences between both samples. IllustrisTNG provides a redshift (or time) discrete sample, whereas the observations cover a continuous range of values. Moreover, in the IllustrisTNG simulation we observe (or follow) the same galaxies for all the redshift samples. This is obviously not the case in the GAMA observations. Additionally, the selection of star-forming galaxies using the BPT diagram is only possible for GAMA. While for the IllustrisTNG simulations we selected only star forming particles and excluded passive galaxies. Finally, Zhao et al. (2020) found differences in the SFR for the different resolution levels of TNG100 and TNG300.

6 SUMMARY AND CONCLUSIONS

We present an analysis of variations in SFR, sSFR, and gas metallicity for group galaxies in the GAMA survey. Groups are selected using the friends-of-friends algorithm as described in the G^{3}C GAMA groups catalogue (Robotham et al. 2011). The galaxies selected present at least four emission lines (Hα, Hβ, [NII]λ6583, and [OIII]λ5007). After AGN discrimination by means of the BPT diagnostic, we end up with 26 174 star forming galaxies. We generated three volume-limited samples to control for evolution and mass variation with redshift due to the Malquimist bias. Variations in the main properties are identified through offsets in the zero-point between control and group samples in the M–Z, M–SFR, and M–sSFR relations. Our main conclusions are given in the following bullet points:

(i) The gas metallicity of low redshift galaxies (V1) and low stellar masses is higher than the control sample by ∼0.05 dex, while group galaxies in the volume V3 show a small decrement in metallicities. Our group sample shows as well a higher metallicity in the highest surface density bin with respect to the control sample by ∼0.08 dex, having the rest of the density bins values comparable with those in the field. These results are in agreement with Ellison et al. (2009). Stripping of low-metallicity gas from the galaxy outskirts, as well as suppression of metal-poor inflows towards the galaxy centre, or even inflow of pre-processed gas from a rich ICM are key drivers of the enhancement of gas metallicity (e.g. Bahé et al. 2017).

(ii) SFR and sSFR are higher in groups compared to field galaxies in the samples V1 and V2, indicating that mechanisms enhancing SFR are already dominant here, while those quenching them take longer times to be noticeable.

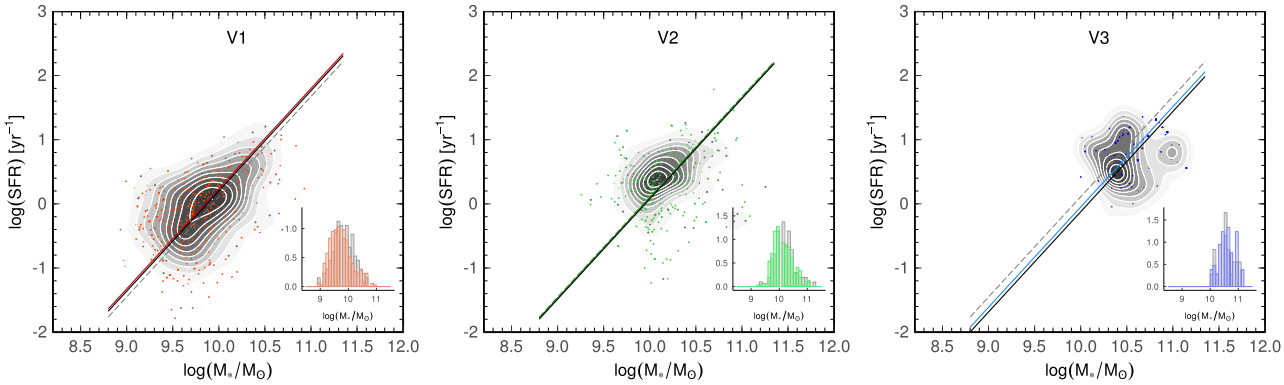

Figure 18. M–SFR relationship for the three volume-limited samples from simulations (see the text) V1, V2, V3 (left-hand panel, centre, right-hand panel, respectively). The grey dots represent control group galaxies, and coloured dots (red, green, blue for V1, V2, V3, respectively), group galaxies. The black line represents the best fit for the control subsample whereas the coloured line is the fit for the group galaxies subsample. The grey dashed line is the fiducial fit to the joint set of the control samples. Inset histograms represent the mass distributions of the groups (coloured) and control (grey) galaxies.

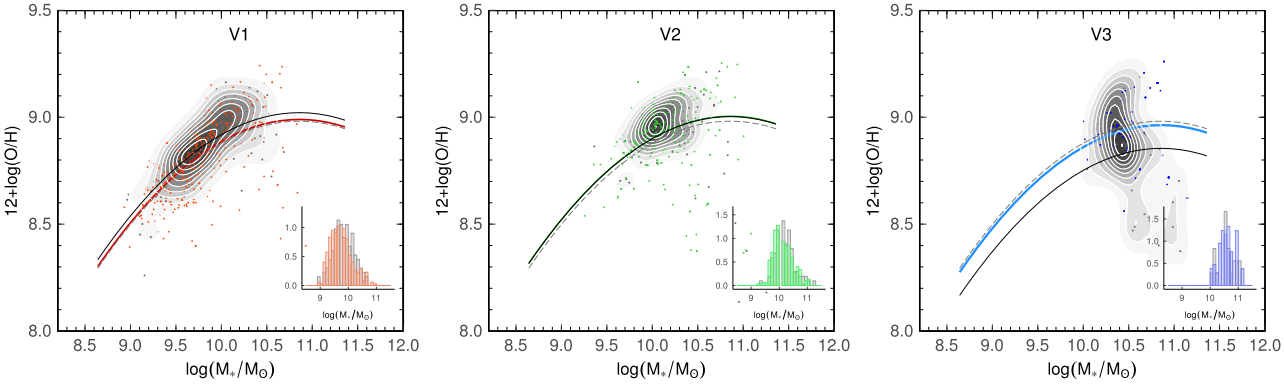

Figure 19. M–Z relations for the three volumes from simulations. Symbols and lines similar to Fig. 18.

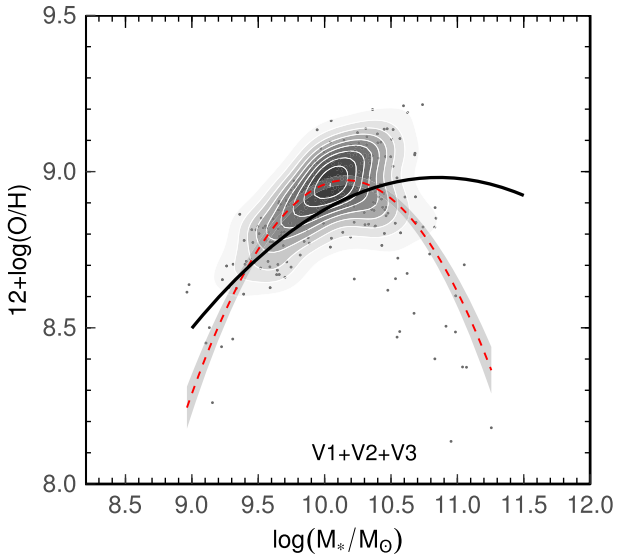

Figure 20. M–Z relation for control galaxies from IlustrisTNG. The grey data represent data from the V1, V2, and V3 volumes together. The red line is the best-fitting to the simulated data. The black line is the best-fitting based on the GAMA data (also shown as grey dashed lines in Fig. 19).

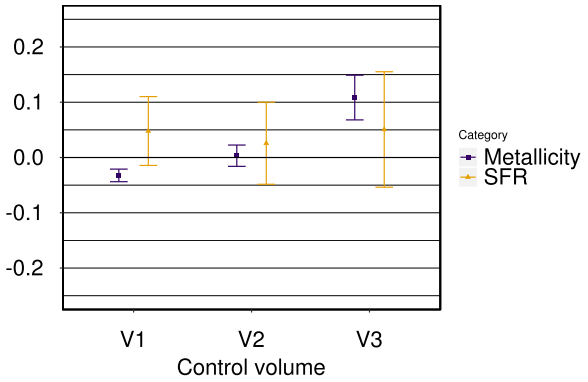

Figure 21. Differences for the zero-point between group and control galaxies in the simulation TNG300. The differences and 1-σ error bars in metallicity and SFR are colour coded as in Fig. 9.

(iii) Our full sample was analysed in bins of group-centric distance, local density, Σ_5, and stellar mass. We find that the highest enhancements in SFR and sSFR, ∼0.3 and 0.4, respectively, are found for galaxies with the lower local densities.

(iv) Contrary to previous authors that find an SFR quenched for galaxies at highest local densities or close group-centric distances, we find small enhancements in SFR of ∼0.1 dex. This difference can be explained as our sample of group galaxies is composed of

galaxies with strong emission lines and hence late-type morphologies, excluding the low-SFR and passive systems that drive previous results showing the suppression in SFR.

(v) The only signs of quenching in our samples are found for massive galaxies, either when the whole sample is used (Fig. 14), with a volume-limited sample of luminous/massive galaxies throughout our whole redshift range (Fig. 15), or when individual volume-limited samples are considered (Figs 9 and 16). Therefore, our data suggests the stellar mass is the benchmark to identify quenching in galaxies with strong emission lines.

(vi) In contrast, lower gas metallicities are found for galaxies at high group-centric distances (Fig. 11). It is likely that this is connected to the accretion of H I rich galaxies residing preferentially in the outskirts, also responsible for the observed enhancement in SFR at the same group-centric distances.

(vii) We tried to reproduce our observational results with group galaxies from the IlustrisTNG simulations, and successfully recovered the general trends for M–Z and M–SFR. However, even though we used the same methodology, we did not find the same quantitative differences as with the observational GAMA data. This discrepancy can be attributed to the discrete outputs for different redshift values in the simulation.

ACKNOWLEDGEMENTS

GAMA is a joint European-Australasian project based around a spectroscopic campaign using the Anglo-Australian Telescope. The GAMA input catalogue is based on data taken from the Sloan Digital Sky Survey and the UKIRT Infrared Deep Sky Survey. Complementary imaging of the GAMA regions is being obtained by a number of independent survey programs including GALEX MIS, VST KIDS, VISTA VIKING, WISE, Herschel-ATLAS, GMRT, and ASKAP providing UV to radio coverage. GAMA is funded by the STFC (UK), the ARC (Australia), the AAO, and the participating institutions. The GAMA website is http://www.gama-survey.org/. This work was supported by the project 'Evolution of Galaxies', of reference AYA2017–88007–C3–2–P, within the 'Plan Estatal de Investigación Científica y Técnica y de Innovación (2017-2020)' of the 'Agencia Estatal de Investigación del Ministerio de Ciencia, Innovación y Universidades'. APG is also supported by the Spanish State Research Agency grant MDM-2017- 0737 (Unidad de Excelencia María de Maeztu CAB). MALL acknowledges support from the Carlsberg Foundation via a Semper Ardens grant (CF15-0384).

DATA AVAILABILITY

All observational data from the GAMA Project used in this work is publicly available at http://www.gama-survey.org/dr3/. Results from the IllustrisTNG simulation are publicly available at https://www.tng-project.org.

REFERENCES

Abazajian K. N. et al., 2009, ApJS, 182, 543
Allen R. J., Kacprzak G. G., Glazebrook K., Tran K.-V. H., Spitler L. R., Straatman C. M. S., Cowley M., Nanayakkara T., 2016, ApJ, 826, 60
Alonso M. S., Lambas D. G., Tissera P., Coldwell G., 2007, MNRAS, 375, 1017
Bahé Y. M., Schaye J., Crain R. A., McCarthy I. G., Bower R. G., Theuns T., McGee S. L., Trayford J. W., 2017, MNRAS, 464, 508
Baldry I. K., Balogh M. L., Bower R. G., Glazebrook K., Nichol R. C., Bamford S. P., Budavari T., 2006, MNRAS, 373, 469
Baldry I. K. et al., 2010, MNRAS, 404, 86
Baldwin J. A., Phillips M. M., Terlevich R., 1981, PASP, 93, 5
Balogh M. L., Morris S. L., Yee H. K. C., Carlberg R. G., Ellingson E., 1997, ApJ, 488, L75
Bamford S. P., Milvang-Jensen B., Aragón-Salamanca A., 2007, MNRAS, 378, L6
Barsanti S. et al., 2018, ApJ, 857, 71
Barton E. J., Geller M. J., Kenyon S. J., 2000, ApJ, 530, 660
Biffi V. et al., 2017, MNRAS, 468, 531
Brooks A. M., Governato F., Booth C. M., Willman B., Gardner J. P., Wadsley J., Stinson G., Quinn T., 2007, ApJ, 655, L17
Bruzual G., Charlot S., 2003, MNRAS, 344, 1000
Busha M. T., Evrard A. E., Adams F. C., Wechsler R. H., 2005, MNRAS, 363, L11
Calvi R., Poggianti B. M., Fasano G., Vulcani B., 2012, MNRAS, 419, L14
Calvi R., Vulcani B., Poggianti B. M., Moretti A., Fritz J., Fasano G., 2018, MNRAS, 481, 3456
Cardelli J. A., Clayton G. C., Mathis J. S., 1989, ApJ, 345, 245
Corcho-Caballero P., Ascasibar Y., López-Sánchez Á. R., 2020, MNRAS, 499, 573
Couch W. J., Balogh M. L., Bower R. G., Smail I., Glazebrook K., Taylor M., 2001, ApJ, 549, 820
Davé R., Thompson R., Hopkins P. F., 2016, MNRAS, 462, 3265
Davé R., Rafieferantsoa M. H., Thompson R. J., Hopkins P. F., 2017, MNRAS, 467, 115
Davies L. J. M. et al., 2015, MNRAS, 452, 616
De Rossi M. E., Bower R. G., Font A. S., Schaye T., 2018, Bol. Asoc. Argentina Astron. Argentina, 60, 121
Di Matteo T., Springel V., Hernquist L., 2005, Nature, 433, 604
Dressler A., 1980, ApJ, 236, 351
Dressler A. et al., 1997, ApJ, 490, 577
Driver S. P. et al., 2011, MNRAS, 413, 971
Eke V. R., Baugh C. M., Cole S., Frenk C. S., King H. M., Peacock J. A., 2005, MNRAS, 362, 1233
Ellison S. L., Patton D. R., Simard L., McConnachie A. W., 2008, AJ, 135, 1877
Ellison S. L., Simard L., Cowan N. B., Baldry I. K., Patton D. R., McConnachie A. W., 2009, MNRAS, 396, 1257
Ellison S. L., Viswanathan A., Patton D. R., Bottrell C., McConnachie A. W., Gwyn S., Cuillandre J.-C., 2019, MNRAS, 487, 2491
Finlator K., Davé R., 2008, MNRAS, 385, 2181
Furlong M. et al., 2015, MNRAS, 450, 4486
Garduño L. E., Lara-López M. A., López-Cruz O., Hopkins A. M., Owers M. S., Pimbblet K. A., Holwerda B. W., 2021, MNRAS, 501, 2969
Genel S., 2016, ApJ, 822, 107
Gordon Y. A. et al., 2017, MNRAS, 465, 2671
Gordon Y. A. et al., 2018, MNRAS, 475, 4223
Goto T., Yamauchi C., Fujita Y., Okamura S., Sekiguchi M., Smail I., Bernardi M., Gomez P. L., 2003, MNRAS, 346, 601
Gunawardhana M. L. P. et al., 2011, MNRAS, 415, 1647
Gunn J. E., Gott J. Richard I., 1972, ApJ, 176, 1
Gupta A. et al., 2018, MNRAS, 477, L35
Haines C. P. et al., 2015, ApJ, 806, 101
Hess K. M., Wilcots E. M., 2013, AJ, 146, 124
Hopkins A. M. et al., 2013, MNRAS, 430, 2047
Hopkins P. F., Hernquist L., Cox T. J., Di Matteo T., Robertson B., Springel V., 2006, ApJS, 163, 1
Hsieh B. C. et al., 2017, ApJ, 851, L24
Hwang H. S., Shin J., Song H., 2019, MNRAS, 489, 339
Karim A., Schinnerer E., 2011, ASPC, 446, 269
Kauffmann G. et al., 2003, MNRAS, 346, 1055
Kewley L. J., Ellison S. L., 2008, ApJ, 681, 1183
Kewley L. J., Dopita M. A., Sutherland R. S., Heisler C. A., Trevena J., 2001, ApJ, 556, 121
Kewley L. J., Geller M. J., Barton E. J., 2006, AJ, 131, 2004
Kulas K. R. et al., 2013, ApJ, 774, 130
Lambas D. G., Tissera P. B., Alonso M. S., Coldwell G., 2003, MNRAS, 346, 1189

Lara-López M. A., Cepa J., Bongiovanni A., Castañeda H., Pérez García A. M., Fernández Lorenzo M., Póvic M., Sánchez-Portal M., 2009a, A&A, 493, L5
Lara-López M. A., Cepa J., Bongiovanni A., Pérez García A. M., Castañeda H., Fernández Lorenzo M., Pović M., Sánchez-Portal M., 2009b, A&A, 505, 529
Lara-López M. A., Bongiovanni A., Cepa J., Pérez García A. M., Sánchez-Portal M., Castañeda H. O., Fernández Lorenzo M., Pović M., 2010, A&A, 519, A31
Lara-López M. A. et al., 2013, MNRAS, 434, 451
Lara-López M. A., De Rossi M. E., Pilyugin L. S., Gallazzi A., Hughes T. M., Zinchenko I. A., 2019, MNRAS, 490, 868
Lequeux J., Peimbert M., Rayo J. F., Serrano A., Torres-Peimbert S., 1979, A&A, 500, 145
Lewis I. et al., 2002, MNRAS, 334, 673
Lilly S. J. et al., 2007, ApJS, 172, 70
Liske J. et al., 2015, MNRAS, 452, 2087
Marinacci F. et al., 2018, MNRAS, 480, 5113
McDonald M. et al., 2016, ApJ, 826, 124
McNaught-Roberts T. et al., 2014, MNRAS, 445, 2125
Merson A. I. et al., 2013, MNRAS, 429, 556
Moore B., Katz N., Lake G., Dressler A., Oemler A., 1996, Nature, 379, 613
Moutard T., Sawicki M., Arnouts S., Golob A., Malavasi N., Adami C., Coupon J., Ilbert O., 2018, MNRAS, 479, 2147
Muldrew S. I. et al., 2011, MNRAS, 419, 2670–2682
Naiman J. P. et al., 2018, MNRAS, 477, 1206
Nelson D. et al., 2018, MNRAS, 475, 624
Nikolic B., Cullen H., Alexander P., 2004, MNRAS, 355, 874
Oman K. A., Hudson M. J., 2016, MNRAS, 463, 3083
Osterbrock D. E., 1989, Astrophysics of Gaseous Nebulae and Active Galactic Nuclei. A. University Science Books, Herndon, VA
Pan H.-A. et al., 2019, ApJ, 881, 119
Patton D. R. et al., 2020, MNRAS, 494, 4969
Peng Y., Maiolino R., 2014, MNRAS, 443, 3643
Peng Y., Maiolino R., Cochrane R., 2015, Nature, 521, 192
Peng Y.-J. et al., 2010, ApJ, 721, 193
Peng Y.-J., Lilly S. J., Renzini A., Carollo M., 2012, ApJ, 757, 4
Pettini M., Pagel B. E. J., 2004, MNRAS, 348, L59
Pillepich A. et al., 2018, MNRAS, 475, 648
Pilyugin L. S., Thuan T. X., 2011, ApJ, 726, L23
Pilyugin L. S. et al., 2013, MNRAS, 432, 1217
Poggianti B. M., Smail I., Dressler A., Couch W. J., Barger A. J., Butcher H., Ellis R. S., Oemler Augustus J., 1999, ApJ, 518, 576
Postman M. et al., 2005, ApJ, 623, 721
Postman M., Geller M. J., 1984, ApJ, 281, 95
Robotham A. S. G. et al., 2011, MNRAS, 416, 2640
Robotham A. S. G., Obreschkow D., 2015, Publ. Astron. Soc. Austr, 32, e033
Sarzi M. et al., 2006, MNRAS, 366, 1151
Schaller M., Dalla Vecchia C., Schaye J., Bower R. G., Theuns T., Crain R. A., Furlong M., McCarthy I. G., 2015, MNRAS, 454, 2277
Schawinski K. et al., 2014, MNRAS, 440, 889
Scudder J. M., Ellison S. L., Torrey P., Patton D. R., Mendel J. T., 2012, MNRAS, 426, 549
Scudder J. M., Ellison S. L., Momjian E., Rosenberg J. L., Torrey P., Patton D. R., Fertig D., Mendel J. T., 2015, MNRAS, 449, 3719
Semczuk M., Lokas E. L., D'Onghia E., Athanassoula E., Debattista V. P., Hernquist L., 2020, MNRAS, 498, 3535
Shah E. A. et al., 2020, ApJ, 904, 107
Sharp R. et al., 2006, in Proc. SPIE Conf. Ser. Vol. 6269, Performance of AAOmega: the AAT multi-purpose fiber-fed spectrograph. A. SPIE, Bellingham, p. 62690G
Shimakawa R., Kodama T., Tadaki K., Hayashi M., Koyama Y.and Tanaka I., 2015, MNRAS, 448, 666
Spitoni E., Calura F., Matteucci F., Recchi S., 2010, A&A, 514, A73
Springel V. et al., 2018, MNRAS, 475, 676
Taylor E. N. et al., 2011, MNRAS, 418, 1587
Torrey P. et al., 2018, MNRAS, 477, L16
Torrey P. et al., 2019, MNRAS, 484, 5587
Tremonti C. A. et al., 2004, ApJ, 613, 898
Trussler J., Maiolino R., Maraston C., Peng Y., Thomas D., Goddard D., Lian J., 2020, MNRAS, 491, 5406
Valentino F. et al., 2015, ApJ, 801, 132
Vogelsberger M. et al., 2018, MNRAS, 474, 2073
von der Linden A., Wild V., Kauffmann G., White S. D. M., Weinmann S., 2010, MNRAS, 404, 1231
Vulcani B., Poggianti B. M., Finn R. A., Rudnick G., Desai V., Bamford S., 2010, ApJ, 710, L1
Wang L. et al., 2018, A&A, 618, A1
Wetzel A. R., Tinker J. L., Conroy C., van den Bosch F. C., 2013, MNRAS, 432, 336
Wijesinghe D. B. et al., 2012, MNRAS, 423, 3679
Woods D. F., Geller M. J., 2007, AJ, 134, 527
Wu P.-F., Zahid H. J., Hwang H. S., Geller M. J., 2017, MNRAS, 468, 1881
Wuyts S. et al., 2011, ApJ, 742, 96
York D. G. et al., 2000, AJ, 120, 1579
Yun K. et al., 2019, MNRAS, 483, 1042
Zhao P., Xu H., Katsianis A., Yang X., 2020, Res. Astron. Astrophys., 20, 195

This paper has been typeset from a TEX/LATEX file prepared by the author.